SPED Light Sheet Microscopy: Fast Mapping of Biological System Structure and Function

Raju Tomer,[1,2] Matthew Lovett-Barron,[1,2] Isaac Kauvar,[2,3] Aaron Andalman,[1,2] Vanessa M. Burns,[2,4] Sethuraman Sankaran,[2] Logan Grosenick,[2] Michael Broxton,[5] Samuel Yang,[2,3] and Karl Deisseroth[1,2,6,7,*]
[1]Department of Bioengineering
[2]CNC Program
[3]Department of Electrical Engineering
[4]Department of Chemical and Systems Biology
[5]Department of Computer Science
[6]Howard Hughes Medical Institute
[7]Department of Psychiatry and Behavioral Sciences
Stanford University, Stanford, CA 94305, USA
*Correspondence: deissero@stanford.edu
http://dx.doi.org/10.1016/j.cell.2015.11.061

SUMMARY

The goal of understanding living nervous systems has driven interest in high-speed and large field-of-view volumetric imaging at cellular resolution. Light sheet microscopy approaches have emerged for cellular-resolution functional brain imaging in small organisms such as larval zebrafish, but remain fundamentally limited in speed. Here, we have developed SPED light sheet microscopy, which combines large volumetric field-of-view via an extended depth of field with the optical sectioning of light sheet microscopy, thereby eliminating the need to physically scan detection objectives for volumetric imaging. SPED enables scanning of thousands of volumes-per-second, limited only by camera acquisition rate, through the harnessing of optical mechanisms that normally result in unwanted spherical aberrations. We demonstrate capabilities of SPED microscopy by performing fast sub-cellular resolution imaging of CLARITY mouse brains and cellular-resolution volumetric Ca^{2+} imaging of entire zebrafish nervous systems. Together, SPED light sheet methods enable high-speed cellular-resolution volumetric mapping of biological system structure and function.

INTRODUCTION

Mapping cellular activity across entire vertebrate nervous systems at high spatiotemporal resolution is a methodology with the potential to substantially advance our understanding of the neural mechanisms driving behavior, including sensation, action, internal states, and cognition. Electrophysiological approaches have generated critical insights into nervous system function,

but these methods are generally limited in the number of neurons that can be recorded simultaneously. The development of genetic tools for optical observation (Chen et al., 2013) and intervention (Deisseroth, 2015) of neuronal activity have expanded the spatial extent of neural circuits that can be studied, allowing for analysis of information exchange within large ensembles of active neurons in intact, behaving animals. In order to capitalize on this ability to address large neural populations in intact nervous systems, high-speed and high-resolution volumetric imaging methods will be required to interact with the intact volumes over large fields-of-view. The approach of light sheet microscopy (LSM; Stelzer, 2015) has emerged as a useful platform for meeting these goals, and has already been used for functional neural imaging of ex vivo mouse vomeronasal organ (Holekamp et al., 2008), portions of mouse neocortex (Bouchard et al., 2015), and the entirety of small larval nervous systems of *Drosophila* (Chhetri et al., 2015; Lemon et al., 2015) and the larval zebrafish brain (Ahrens et al., 2013; Chhetri et al., 2015; Freeman et al., 2014; Panier et al., 2013; Vladimirov et al., 2014) at up to 1–3 volumes per second. Introduced more than 100 years ago (Siedentopf and Zsigmondy, 1903), LSM has seen a revival in interest over the last two decades with successful applications to neural activity mapping (Freeman, 2015; Keller et al., 2015), developmental biology (Huisken et al., 2004; Keller et al., 2008; Preibisch et al., 2010; Reynaud et al., 2015; Wu et al., 2013), cell biology (Gao et al., 2012; Planchon et al., 2011), and high-resolution whole-brain neuroanatomy (Lerner et al., 2015; Tomer et al., 2014).

The essential idea of LSM involves illumination of a sample with a thin sheet of light and detection of the emitted signal with an orthogonally arranged wide-field detection arm. Critical for in vivo imaging applications, this configuration limits photobleaching and toxicity by minimizing the energy load of the excitation light on the sample and allows for fast imaging by simultaneous sampling of an entire plane that can be visualized with modern sCMOS or CCD cameras. Volumetric data can be acquired this way by either scanning the sample through a stationary light sheet/detection objective, or by moving the light

sheet/objective synchronously to scan a stationary sample. The latter mode allows fast volumetric imaging and has been successfully used for functional imaging experiments (Ahrens et al., 2013; Holekamp et al., 2008). However, the volumetric imaging speed of this approach is fundamentally limited by the requirement to move heavy detection objectives, which are mounted on piezo motors with range of motion limited to a few hundred microns. Several distinct approaches are under exploration to address this limitation. Huisken and colleagues (Fahrbach et al., 2013) used electrically tunable lenses to move the focal plane of the stationary detection objective without physically moving the objective itself. Hillman and colleagues devised an approach (Bouchard et al., 2015), building upon oblique plane microscopy (Dunsby, 2008), to generate an oblique light sheet through the detection objective itself, which is then swept through the sample for volumetric imaging. Both of these approaches improve imaging speed but suffer from optical artifacts (especially beyond the native focal plane or point), are generally restricted to small sample depths, and require complex instrumentation and alignment procedures.

Here, we introduce a conceptually distinct microscopy approach, SPED (SPherical-aberration-assisted Extended Depth-of-field) light sheet microscopy, which turns spherical aberration into an advantage by combining the large volumetric field of view of an extended depth of field with the optical sectioning of light sheet microscopy, thereby eliminating the need to physically scan the detection objective for volumetric imaging while maintaining spatial resolution. At the core of SPED light sheet microscopy is a unique and scalable method for extending the depth of field, by building upon the optical mechanisms that induce spherical aberrations. An image volume is acquired by scanning the light sheet only (using galvanometer scanners) rather than the specimen or objective, thus providing the capability to scan several thousands of volumes in a second: imaging speed is therefore only limited by the camera rate of acquisition of illuminated planes. We demonstrate the capability of SPED light sheet microscopy by imaging 1-mm-thick CLARITY (Chung et al., 2013; Tomer et al., 2014) mouse brain samples at sub-cellular resolution, and by recording neural activity across the entire brain or nervous system (including the full spinal cord) of 10 days post-fertilization (dpf) larval zebrafish at 12 volumes per second and >6 volumes per second, respectively. The resulting datasets were readily adapted to automated standard image segmentation and quantitative analysis pipelines, demonstrating fast and practical cellular resolution capability across intact vertebrate nervous systems.

RESULTS

SPED Light Sheet Microscopy

We combined extension of depth-of-field with the optical sectioning of LSM to develop SPED light sheet microscopy (Figures 1, 2, and S1). An important feature of LSM is that the final system point spread function (PSF) is the intersection of light sheet thickness and detection objective PSF (Figure 1A); the lateral resolution is thus determined by detection objective numerical aperture (NA), and the axial resolution by light sheet thickness. We hypothesized that by extending the axial extent

of the detection PSF (i.e., the depth of field), while maintaining the lateral extent (i.e., x-y resolution), we could perform high-resolution and high-speed volumetric imaging by only scanning a thin light sheet in the z axis, while bypassing the relatively slow process of synchronously moving the heavy detection objective with a piezo motor.

To implement this approach, we first sought to design a scalable method for extending the depth of field of an objective used to image a large intact tissue volume. Several related methods exist, including the use of a cubic phase mask (Quirin et al., 2014; Quirin et al., 2013) behind the detection objective. This method extends the axial extent of the PSF by a few hundred microns, but the elongated PSF suffers from non-linear bending; the resulting images are thus not ideally suited to fast, quantitative imaging over large volumes. In addition, for practical applications this method requires specialized deconvolution and complex optical alignment procedures. Therefore, we set out to develop a unique and simple method that would preserve lateral resolution, and would also be scalable to match the large range of imaging depths required by different experimental needs. Building upon the observation that spherical aberration in optical systems often results in PSF elongation, we devised a simple and robust strategy to use a thick block of altered refractive index material (beyond the design specifications of the objective), between the objective and sample, thereby introducing a large yet uniform spherical aberration (Figure 1A). We predicted that this approach could extend the depth-of-field by orders of magnitude while largely maintaining lateral extent of the PSF (Figure S1), since peripheral rays will travel a longer distance in the higher refractive index material compared to central rays, and thus will focus on different points along the axis, resulting in an elongated PSF (Figure S1).

We tested this idea across four different objectives spanning a broad range of specifications: (i) 4×, 0.28 NA, 29.5 mm working distance (WD), air + 5 mm water; (ii) 10×, 0.25 NA, 21 mm WD, air; (iii) 10×, 0.3 NA, 17 mm WD, air; and (iv) 20×, 0.4 NA, 11 mm WD. The WD of the objectives (i.e., the space between the objective and the sample) was filled with a column of liquid with a refractive index of 1.454 (Figures 1A and 2B; Experimental Procedures). As shown in Figure 1B and Movie S1, this approach yielded substantial PSF elongation, compared to the native PSF of each objective in air, while maintaining the lateral extent of the PSF (note that the 4×/0.28 NA objective is designed for air and 5 mm of water column; therefore, the measured PSF in air alone, shown in Figure 1B, has spherical aberrations as expected.) Figure 1C shows quantification of the elongated PSFs showing that the lateral extent remains largely unchanged (top) and that several hundred microns of the elongated PSFs are usable for volumetric imaging (Figure 1C, bottom).

Next, we sought to identify and assess the crucial factors that can be tuned to generate a desired depth of PSF. For this we modeled the SPED system and performed simulations to characterize the relevant parameters (see Figure S2 and Experimental Procedures for Zemax modeling and simulation details). As summarized in Figure 1D and Figures S2B–S2D PSF elongation is dependent on three parameters of the system: thickness of the refractive index block, the refractive index of the block, and the NA of the detection objective. We found that an increase
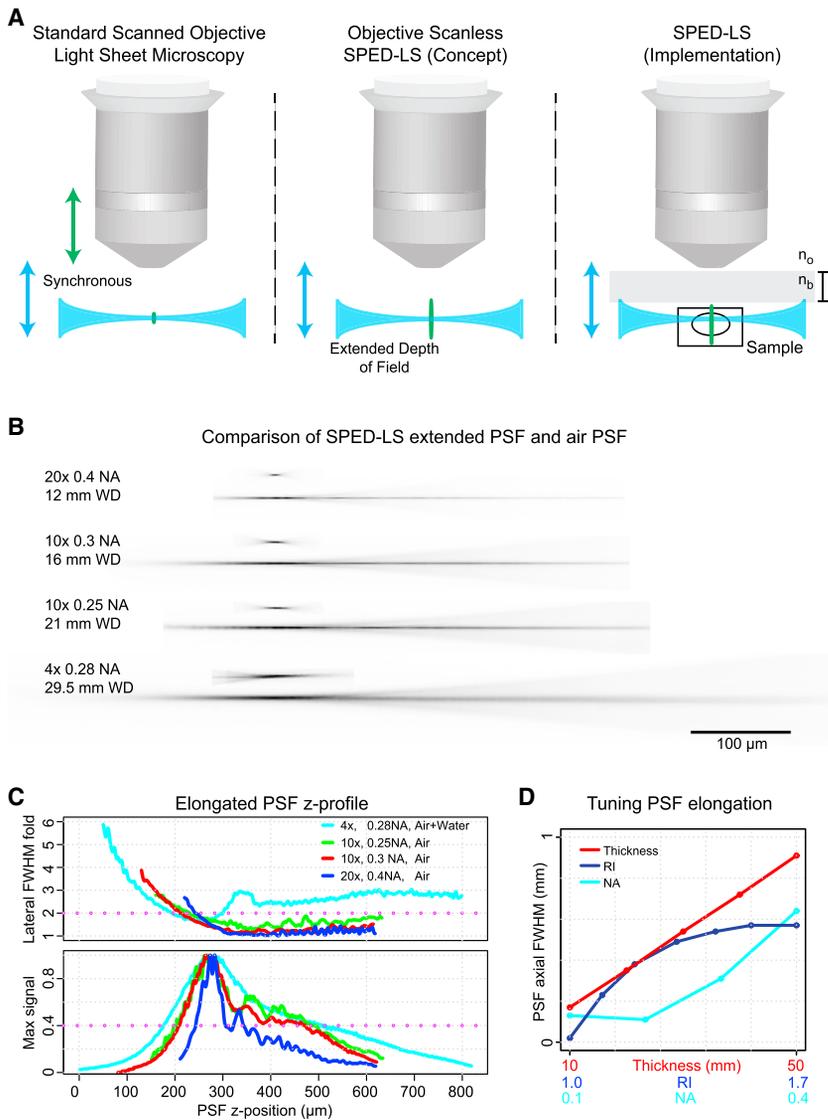
Figure 1. SPherical-Aberration-Assisted Extended Depth-of-Field Light Sheet Microscopy

(A) SPED light sheet concept compared with standard light sheet microscopy (left). In standard light sheet scanning (left), the light sheet and the detection objective are moved synchronously to acquire a 3-dimensional volume. The detection objective is typically mounted on a piezo motor for synchronous z scanning. This design limits the speed of imaging (1–3 volumes per second) because of the mass of the objective and also limits the depth coverage to the piezo travel range (typically a few hundred microns). SPED light sheet scanning (middle) combines a greatly extended depth of field with the optical sectioning of light sheet to provide the capacity to scan thousands of volumes per second. A simple and scalable new method (right) was developed to extend the PSF by orders of magnitude. The method involves placing of a block of higher (or lower) refractive index (n_b) material between the objective and the sample to induce spherical aberrations that elongate the PSF. t, thickness of the block.

(B) A comparison of the native PSF of an objective (measured in air) with the elongated PSF, for four different objectives: Olympus 20×/0.4NA/12 mm WD/Air, Nikon 10×/0.3NA/16 mm WD/Air, Olympus 10×/0.25NA/21 mm WD/Air and Olympus 4×/0.28NA/29.5 mm WD/Air + Water (5 mm). The 3D SPED light sheet empirical PSF measurements for each objective were obtained (Experimental Procedures) by scanning 1 μm-diameter beads and the light sheet synchronously (thus maintaining the uniform illumination of beads) along the z axis, while keeping the detection objective stationary. Individual bead images (n > = 5) were manually extracted from the 3D image volume to generate the final average PSFs. A block of refractive index (1.454) liquid was used to span the entire available working distance of the objective (see Figure S1 for further details).

(C) Characterization of PSF elongation. Top graph plots the fold change in lateral full width at half-maximum (FWHM) of the PSF as function of z position relative to the minimum FWHM of the non-extended air PSF of the same objective. The distribution shows that the lateral extent of the PSF (i.e., lateral resolution) remains largely unchanged for several hundred microns. Note: 4×/0.28 NA objective is designed for air and 5-mm-thick water layer, because of which the PSF measured in air shows aberrations. Bottom graph plots the maximum intensity of the PSF as a function of depth.

(D) Simulations of the SPED microscope were performed to assess the effect of the SPED-LS system parameters: Refractive Index (RI) of the block, its thickness (t) and the NA of the detection objective used. The PSF elongation increases rapidly and reaches saturation with increasing RI of the block, increases linearly with the RI block thickness and increases non-linearly with the increasing NA of the detection objective used. See also Figures S1 and S2 and Movie S1 for details of SPED-LS implementation and PSF simulations.

in the refractive index of the block gives rise to non-linear elongation that saturates as the refractive index approaches 1.7 (Figure S2B). The PSF also can be elongated linearly by increasing the block thickness, the maximum of which is dictated by the WD of the objective (Figure S2C). Finally, an increase in the NA of the detection objective gives rise to a large non-linear elongation (Figure S2D). These results generally were consistent with measured experimental PSFs for the four different objectives, indicating that this framework can serve as a resource for choosing objectives with desired PSF properties and for customizing objectives to induce spherical aberrations.

Deep Cellular and Neurite-Resolution Volumetric Imaging with SPED Light Sheet

To assess the imaging depth and quality of SPED light sheet microscopy, we first set out to perform imaging of a relatively homogenous *Thy1-eYFP* mouse brain sample, clarified using the passive CLARITY protocol (Chung et al., 2013; Tomer et al., 2014). The intact brain sample was imaged using a 4×/0.28NA objective, with the entire WD filled with a block of RI 1.454 liquid. Figures 3A and 3B show signal collected from a 1 mm thick tissue block; the image quality was, however, much reduced at the top and the bottom slices of the stack due in part to the lateral
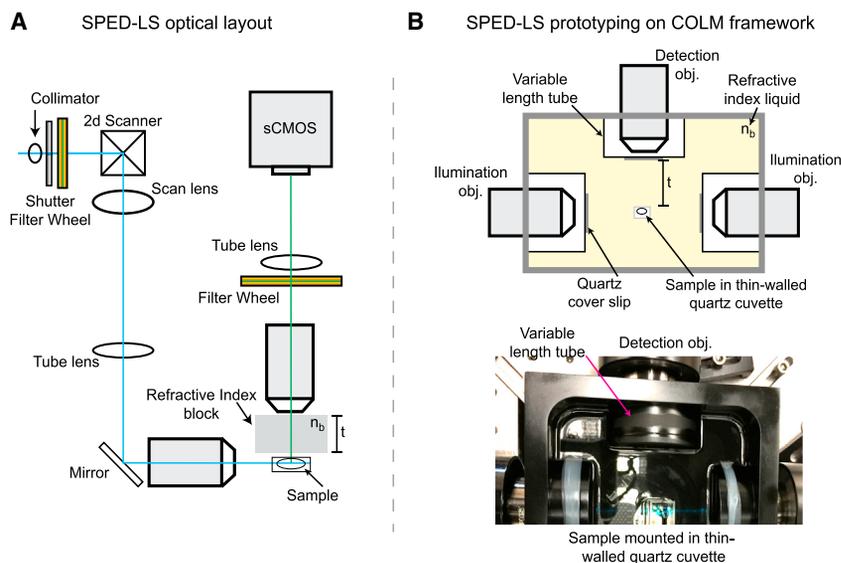
A SPED-LS optical layout

B SPED-LS prototyping on COLM framework

Sample mounted in thin-walled quartz cuvette

Figure 2. SPED Light Sheet Microscopy Implementation

(A) One or two light sheets (second identical light sheet illumination path is not shown in the figure) are created from opposite sides, and the emitted signal is detected with an orthogonal wide-field detection arm. In addition, a block of higher refractive index material is placed between the objective and the sample to induce uniform spherical aberrations for PSF elongation. The illumination arm includes laser source, filter wheel, shutter, x-y 2d galvanometer scanner, scan lens, tube lens, mirror and the illumination objective. The detection arm contains a detection objective, filter wheel, tube lens and sCMOS camera.

(B) First SPED prototype as implemented on the CLARITY-optimized light sheet microscopy (COLM) backbone (Tomer et al., 2014). The large horizontal COLM sample chamber was filled with a specific refractive index (n_b) liquid (1.454 was used for the majority of experiments) to implement the requisite refractive index block for inducing spherical aberration-based PSF extension. Lens tubes (containing quartz glass coverslips for separating the objectives from RI liquid) of varying lengths were used to achieve varying RI block thickness (t). The same effect can be used on the illumination side to achieve increased field of view while maintaining light sheet thickness. Samples were mounted in custom thin-walled (0.5-mm-thick) quartz glass cuvettes. All parts are as described in detail for the COLM framework (Tomer et al., 2014). Although the first prototype is implemented on the COLM backbone, SPED is easily adaptable to any light sheet microscope by incorporating a liquid or solid block of transparent material of defined thickness and refractive index to achieve desired axial elongation of the system PSF.

broadening of the PSF at its axial limits. Therefore, we tested the standard Richardson-Lucy deconvolution method, using the experimentally-measured PSF, and found that much of the information (including neurite-resolution features) could be readily restored, as shown in the comparison of x-y and x-z projections of raw SPED, Richardson-Lucy deconvolved, and standard CLARITY-optimized light sheet microscopy (COLM; Tomer et al., 2014) imaging data (Figures 3, S3, S4, and Movie S2).

Next, we sought to assess imaging quality in live zebrafish larvae, considering that one of the main advantages of SPED microscopy could be fast, complete functional and anatomical imaging of small and relatively transparent model organisms. We acquired image stacks from live, unparalyzed 10 dpf zebrafish larvae expressing the genetically encoded Ca^{2+} indicator GCaMP6s localized to the nucleus (Tg(elavl3:H2B-GCaMP6s); Vladimirov et al., 2014) with two different objectives: 4×/0.28 NA and 10×/0.25 NA. As demonstrated in Figures 4 and S5 and Movies S3 and S4, SPED light sheet allows cellular resolution imaging of entire zebrafish nervous systems. The ability to resolve individual cells throughout the volume was demonstrated by automated image segmentation of the cell nuclei in live imaging datasets, as discussed below and shown in Movie S8.

Comparison of SPED with Light Field Microscopy

We next sought to compare this volumetric imaging method with other methods for fast volumetric imaging. We and others have developed methods such as light field microscopy (LFM; Broxton et al., 2013; Cohen et al., 2014; Grosenick et al., 2009; Levoy et al., 2006; Prevedel et al., 2014) and multifocus microscopy (Abrahamsson et al., 2013; Abrahamsson et al., 2015) to attain high volumetric imaging speeds, in which the entire volume is ac-

quired in a single snapshot. However, this speed comes at the cost of resolution, limits on the sample size, and, in the case of LFM, requirements for complex forms of volumetric deconvolution. SPED microscopy involves scanning the light sheet using only galvanometer scanners, which can run at several KHz, providing the capability to scan thousands of volumes (>1 mm deep) per second while maintaining lateral (determined by detection objective NA) and axial (determined by light sheet thickness) resolution. SPED volumetric imaging speed is thus only limited by the data acquisition rate of sCMOS cameras, which are currently fast and continuously improving.

Cognizant of the potential tradeoffs in real-world application settings, we set out to directly compare the quality of image volumes acquired with LFM and SPED light sheet microscopy. We consecutively imaged a 10 dpf Tg(elavl3:H2B-GCaMP6s) zebrafish larva sample with modern LFM methods (Broxton et al., 2013) and SPED light sheet imaging, using comparable parameters. The LFM image stack was acquired with 500 ms exposure using a 10×/0.6 NA (Olympus) water immersion objective and f/11.36, 100 μm pitch lenslet array, whereas the SPED light sheet volume was acquired with 460 ms exposure at half the NA (10×/0.3NA; Nikon), thus yielding comparable exposure times (500 ms for LFM, 460 ms for SPED light sheet). As shown in Figure 5, SPED light sheet provides higher lateral and axial resolution, even at 12 volumes per second (40 z slices, <100 ms exposure per stack; Figure 6). While SPED light sheet and LFM volumetric imaging rates are both currently limited by the camera acquisition speed (currently ∼1,000 images per second for smaller regions of interest [ROIs]), LFM is fundamentally faster by acquiring the entire volume in each snapshot, compared to the one plane-per-snapshot of SPED light sheet. However, rapidly-improving camera imaging speeds will continue to reduce this difference
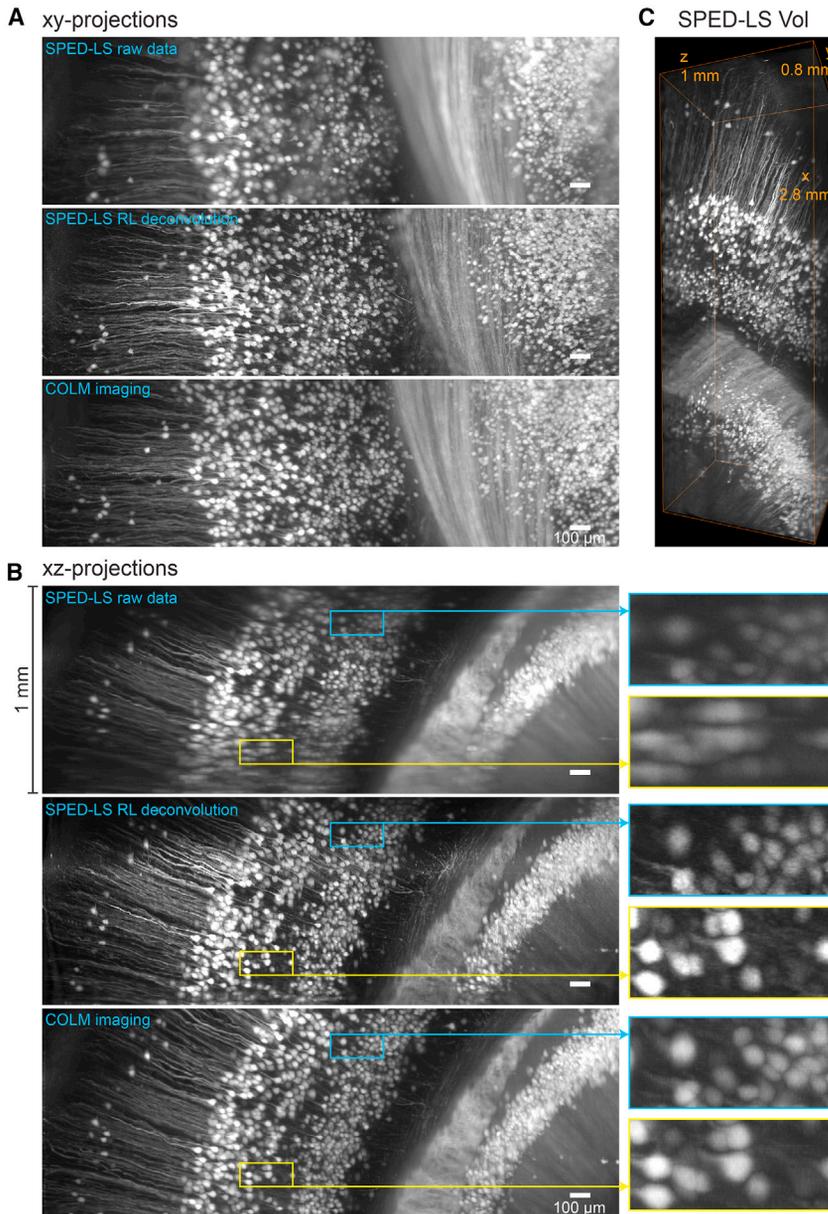
A xy-projections

SPED-LS raw data

SPED-LS RL deconvolution

COLM imaging

100 μm

B xz-projections

SPED-LS raw data

1 mm

SPED-LS RL deconvolution

COLM imaging

100 μm

C SPED-LS Vol

z
1 mm

y
0.8 mm

x
2.8 mm

Figure 3. SPED Light Sheet Imaging Depth Characterization

(A and B) One-millimeter-deep volumes of clarified *Thy1-eYFP* transgenic mouse brain were imaged with SPED light sheet microscopy and with CLARITY-optimized light sheet microscopy (COLM) using a 4×/0.28NA objective to assess the SPED imaging depth. (A) compares the x-y projections and (B) the x-z projections of the raw SPED light sheet image volume, after deconvolution using standard Richardson-Lucy deconvolution with the empirically measured PSF and the standard COLM imaging by moving the sample through stationary light sheet and in-focus detection objective.

(C) Volume rendering of the SPED light sheet volume. Note that because of the low magnification (4×) of the imaging objective, the pixel sampling size was ~1.46 microns which is not sufficient to visualize finer details such as dendritic spines or thinner axons. See also Figure S3 and Movie S2 for detailed comparison of SPED raw and deconvolved data with the COLM imaging, and Figure S4 for a detailed description of the deconvolution pipeline.

tized, but were fully embedded in agarose to limit movement. SPED imaging speed is limited by the speed of current sCMOS cameras at up to 100 full frames per second, but collecting smaller ROIs can provide ~10× higher imaging speed. We found that with the 4× objective, the entire nervous system could be imaged in a single field of view. As the larval zebrafish are longer rostro-caudally than they are wide, we were able to use smaller ROIs (in the direction of the line-by-line readout of the sCMOS camera) to achieve higher frame rates.

We demonstrated SPED light sheet capability in this context by performing 12 volumes/second (0.9 mm × 0.4 mm × 0.2 mm, 40 z slices) imaging of the entire brain and 6.23 volumes/second (3 mm × 0.5 mm × 0.2 mm, 39 z slices) imaging of the entire CNS including the fully extended

to the point at which both methods are limited by the speed of the genetically-encoded activity indicators.

Rapid Cellular-Resolution Functional Imaging of the Entire Zebrafish CNS

To demonstrate the high-speed, cellular-resolution and large field-of-view volumetric imaging capabilities of SPED light sheet, we sought to determine if it would be possible to capture fast cellular-resolution spontaneous activity over the entire larval zebrafish brain, or even the entire CNS (including the brain and the fully extended spinal cord). We used two different objectives, 4×/0.28 NA and 10×/0.25 NA, to perform imaging of 10 dpf Tg(*elavl3:H2B-GCaMP6s*) zebrafish larvae embedded in low melting-point agarose. Zebrafish were not paralyzed or anesthe-

spinal cord; moreover, with 10× magnification we could record 4.14 volumes/second (1.2 mm × 0.43 mm × 0.2 mm, 39 z slices) over the whole brain and proximal spinal cord (Figure 6, S6, and Movies S4, S5, and S6 show visualization of activity across the entire sample). Finally, we found that it was possible to perform automated image segmentation to globally identify labeled cells (see Movie S8 and Experimental Procedures), resulting in datasets well-suited for advanced time-series statistical analyses.

Identifying Co-active Neuronal Populations across the Entire Zebrafish CNS

Many aspects of physiology and behavior result from patterned activity of neurons spanning large parts of the CNS. Therefore, the ability to capture the activity patterns of neurons spread

A Cellular resolution whole nervous system imaging with SPED-LS
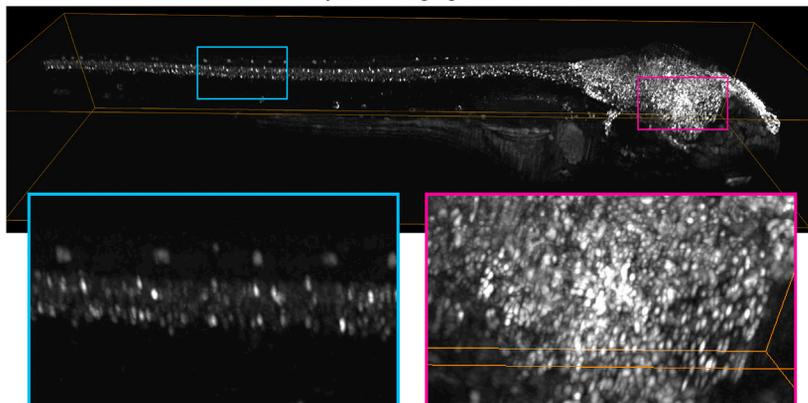
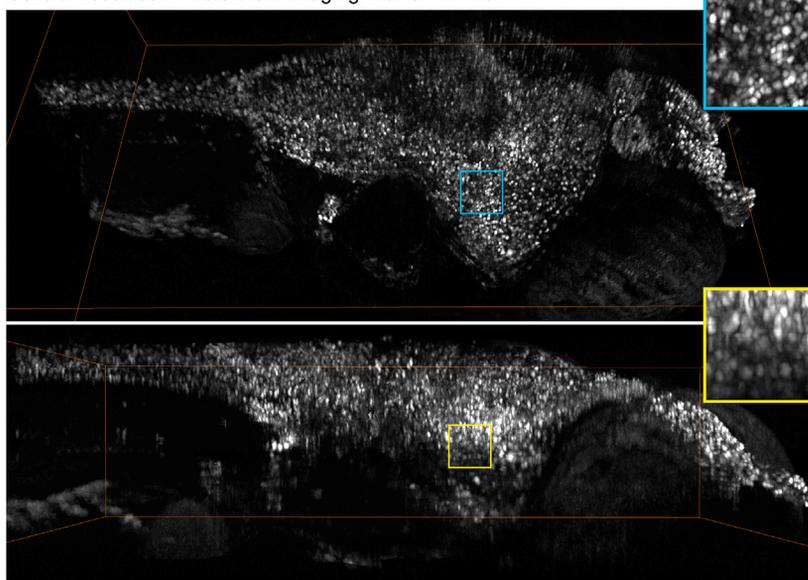**B** Cellular resolution whole brain imaging with SPED-LS

Figure 4. Cellular-Resolution Imaging of the Entire Larval Zebrafish CNS with SPED Light Sheet Microscopy

(A and B) Volume renderings of 10 dpf Tg(*elavl3: H2B-GCaMP6s*) zebrafish larvae imaged with 4×/ 0.28NA (A) and 10×/0.25NA (B) objectives demonstrate the large field of view of SPED microscopy, while maintaining cellular resolution. Cyan and magenta boxes provide magnified views. (A) Image volumes of 10 consecutive time points were collapsed into one volume by taking the maximum values voxel-wise across the recording duration. The bounding box size is 0.75 mm × 2.99 mm × 0.48 mm. (B) Image volumes of 7 consecutive time points were collapsed into one volume by taking the maximum values voxel-wise across the recording duration. The bounding box size is 0.65 mm × 1.20 mm × 0.30 mm. See Movies S3 and S4 for detailed 3-dimensional rendering and Figure S5 for comparison of raw and deconvolved data.

across the entire nervous system is critical for understanding the mechanisms underlying these processes. SPED microscopy, by enabling rapid volumetric imaging of naturally functioning nervous systems, provides a unique opportunity to reveal fundamental principles of nervous system dynamics at cellular resolution. To demonstrate this capability, we employed two commonly used statistical approaches to analyze our datasets of endogenous activity patterns spanning the entire CNS. First, we used principal component analysis (PCA) to collapse highly correlated cells into a lower dimensional space to detect salient population-wide activity patterns (Figure 7). We analyzed ΔF/F traces of active neurons (Experimental Procedures) to reveal population dynamics along the three most significant dimensions (principal components [PCs]), resulting in identification of population synchrony events and the participatory neurons; as shown in Figure 7, the peaks in recovered principal components matched closely with peaks in the neuronal co-activation plots (compare Figures 7A and 7B). To determine the spatial locations and identities of participating neurons, we mapped the PC coef-

ficient magnitudes in the sample space (Figure 6E). In doing so, we identified neurons scattered in spinal cord belonging to all the three PCs (with the majority corresponding to the forebrain PC), identifying long-range (CNS-wide) co-active neurons.

To further reveal the underlying population architecture, we performed independent component analysis (ICA) of the same dataset, resulting in recovery of six independent components (ICs; see Experimental Procedures). By comparing peaks in Figures 7A–7C (dotted lines), we noted that identified IC peaks matched well with PC and co-activation peaks, indicating another effective means of classifying functionally related neurons from large-scale recordings enabled by SPED light sheet microscopy. A comparison of spatial maps of PCA and ICA (Figure 7E) showed consistent populations in forebrain, midbrain, hindbrain, and spinal cord, indicating comparable functional segregation in anatomical space. These observations underscore the capability and value of high-speed neuronal activity measurement across the entire nervous system to reveal global ensembles of functionally related circuitry.

DISCUSSION

Development of tissue clearing technology, and development of optical cellular-activity sensors, together are providing unprecedented opportunities for interrogating large populations of cells spread across entire organ systems or organisms. To help build upon this opportunity, we have here developed SPED light sheet microscopy, which combines the large volumetric field of view of an extended depth of field with the optical sectioning of light sheet microscopy to provide high volumetric imaging speed across a large volume (such as the entire larval zebrafish CNS)
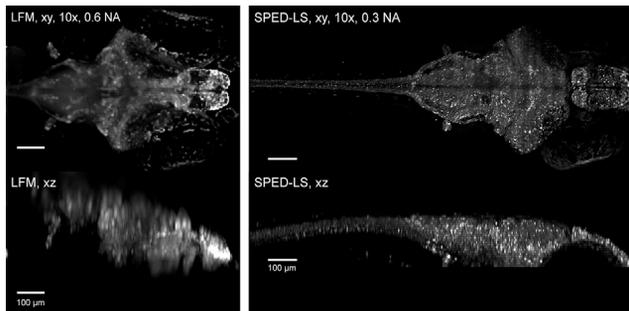
Figure 5. Comparing Resolution of LFM and SPED Light Sheet Methods

Three-dimensional volumes were acquired from a 10 dpf Tg(*elavl3:H2B-GCaMP6s*) zebrafish larva with LFM and SPED light sheet microscopy, using 10×/0.6NA (water immersion, Olympus) objective with 500 ms exposure and 10×/0.3NA (air, Olympus) objective with 460 ms exposure, respectively. SPED light sheet images in Figure 6B were acquired with less than 100 ms exposure/volume, still yielding cellular resolution. Scale bars, 100 μm.

at cellular resolution. At its core, SPED light sheet microscopy consists of a simple and scalable implementation, requiring the introduction of a transparent block of material in the detection path of a standard light sheet microscope, for generating an extended depth of field by inducing uniform spherical aberrations. By choosing the appropriate combination of refractive index, block thickness, and detection objective NA, any desired depth of field can be achieved; for example, we demonstrated sub-cellular resolution structural imaging in clarified mouse brains at 1 mm depth. Although we implemented the first SPED light sheet prototype on the COLM framework (Tomer et al., 2014), which provided particularly easy access to test liquids of different refractive indices and thickness, the same effect may be easily achieved on any standard light sheet microscope (e.g., by using a solid transparent block of given refractive index and thickness). This approach can also be extended to more specialized systems such as 2-photon light sheet (Truong et al., 2011; Wolf et al., 2015), lattice light sheet (Chen et al., 2014), Bessel light sheet (Planchon et al., 2011), multi-direction illumination configurations (Vladimirov et al., 2014), dual inverted SPIM (diSPIM; Wu et al., 2013), openSPIM (Pitrone et al., 2013) and IsoView microscopy (Chhetri et al., 2015). Moreover, the PSF extension method described here may also be useful on the light sheet illumination side to maintain light sheet thickness over a large field of view.

SPED light sheet microscopy provides high spatial resolution comparable to standard light sheet microscopes, while providing the potential to scan more than 1,000 volumes per second, as a galvanometer scanner can scan a light sheet through an entire volume in less than a millisecond. The speed of this method is therefore only limited by camera acquisition rates, which are rapidly improving. In comparison to the IsoView light sheet microscope (Chhetri et al., 2015), it may be noted that SPED microscopy is simpler and less expensive to implement, with faster imaging speeds at similar image quality, and can (if desired) be similarly integrated with four orthogonal detection-arm-based configurations to yield higher axial resolution. Here, we used SPED light sheet microscopy to achieve cellular-resolu-

tion functional imaging of the entire larval zebrafish CNS at up to an order of magnitude greater speed than previously published methods; more broadly, the features of SPED light sheet microscopy may be ideally suited for rapid functional and/or structural imaging of small, relatively transparent model organisms such as zebrafish larvae, the isolated nervous system of *Drosophila* larvae, and *C. elegans*, as well as of larger tissues including those of mammalian origin (after clearing to reduce light scattering, while preserving biomolecules for labeling). Indeed, the initial construction of acrylamide-related polymer hydrogels from within, and covalently linked to, biological tissues for selective preservation or elimination of distinct tissue elements (Chung et al., 2013; Tomer et al., 2014) was subsequently applied in diverse approaches (Chung et al., 2013; Tomer et al., 2014; Chen et al., 2015; present paper), including with expansion of the composite tissue-polymer hybrid itself (Tomer et al., 2014; Chen et al., 2015) and with new approaches to microscopy that leverage the unique properties of hydrogel-tissue composites (Tomer et al., 2014; Chen et al., 2015; present paper, Figure 3). Adapting the unique properties of SPED light sheet microscopy for transparent or semi-transparent biological samples to increase imaging resolution and speed may thus find broad application in biology.

While SPED light sheet can achieve fast imaging rates at high spatial resolution, methods such as LFM and multi-focal microscopy achieve faster volumetric imaging, because these methods acquire an entire volume simultaneously in a single snapshot. However, SPED has no fundamental limitation in achieving much greater speeds as sCMOS camera technology advances rapidly, while LFM, though operating at higher speeds, currently remains limited in spatial resolution. It is worth noting that although the SPED light sheet PSF is spread at the detector (Figure S1C), nearly all of the photons will arrive at the sensor no matter where the light sheet is (Figure S1C), providing good SNR properties. Finally, the extended depth of field, and hence the SNR, can be adapted in SPED light sheet to a desired range for a given preparation; this is a feature lacking in other volumetric imaging methods such as multi-focal volumetric microscopy (Abrahamsson et al., 2013). Next steps in SPED light sheet may involve decoupling the SNR and PSF depth of field extension, further increasing the depth of field by 2-fold using two opposite-side detection arms, and further PSF engineering through objective design. Indeed, with imaging depths of up to 1 mm already demonstrated, it will be straightforward to extend the SPED PSF further by choosing appropriate optical parameters (as shown in Figure 1), and custom objectives for inducing spherical aberrations will further enhance SPED capabilities.

SPED light sheet microscopy may be particularly useful for neuroscience research in allowing both functional and structural imaging at high speeds and may be integrated with complementary optics for optogenetics to perform simultaneous recording and control of neural activity across the entire vertebrate nervous system. As shown here, SPED already enables CNS-wide identification of distinct classes of fast neuronal population dynamics as well as rapid high-resolution mapping of the structural architecture of large intact clarified biological tissues. But developmental and cell biology experiments also can require rapid capturing of events (such as cellular division, dynamics of
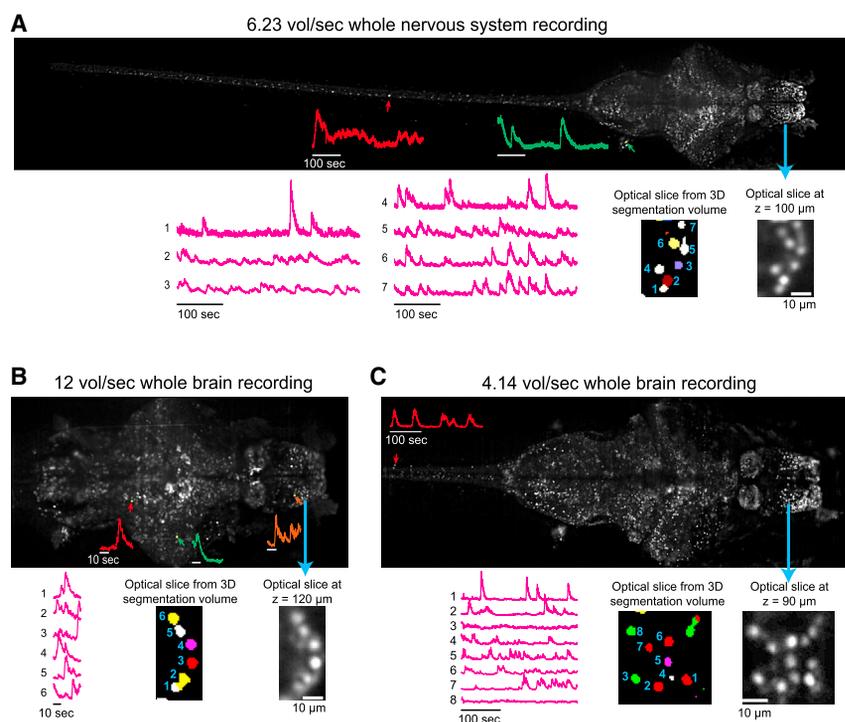
A

6.23 vol/sec whole nervous system recording

100 sec

1
2
3

100 sec

4
5
6
7

100 sec

Optical slice from 3D segmentation volume

Optical slice at z = 100 μm

10 μm

B 12 vol/sec whole brain recording

10 sec

10 sec

1
2
3
4
5
6

Optical slice from 3D segmentation volume

Optical slice at z = 120 μm

10 μm

C 4.14 vol/sec whole brain recording

100 sec

10 sec

1
2
3
4
5
6
7
8

100 sec

Optical slice from 3D segmentation volume

Optical slice at z = 90 μm

10 μm

Figure 6. Rapid Cellular-Resolution Functional Mapping of the Entire Larval Zebrafish Nervous System

(A–C) The camera-frame-rate limited volumetric imaging speed of SPED light sheet is demonstrated by performing rapid cellular-resolution functional mapping of the nervous system of 10 dpf Tg(*elavl3:H2B-GCaMP6s*) zebrafish larvae. Three smaller ROIs of the camera frame were used to image: (A) the entire nervous system with a 4×/0.28 NA objective at 6.23 volumes per second (3 mm × 0.5 mm × 0.2 mm, 39 z slices), (B) the whole brain with a 4×/0.28NA objective at 12 volumes per second (0.9 mm × 0.4 mm × 0.2 mm, 40 z slices), and (C) the whole brain and anterior spinal cord with a 10×/0.25NA objective at 4.14 volumes per second (1.2 mm × 0.43 mm × 0.2 mm, 39 z slices). The maximum intensity projection images were generated from a collapsed 3D volume generated by voxel-wise standard deviation (SD) across the entire recording durations. Cellular resolution is demonstrated by several examples of activity traces (ΔF/F versus time) of neurons marked by colored arrows, and of neighboring cells shown in optical slices from respective volumes and their automated 3D segmentation. See Figure S6 for the top 99 example activity traces (ordered according to the variance across time) from the three datasets. Movies S5, S6, S7 exhibit the activity time series (ΔF/F versus time) of these datasets, and Movie S8 shows details of automated 3D segmentation.

signaling pathways, release of neurotransmitters and tissue morphogenesis) in three dimensions while minimizing imaging energy load on the sample. Indeed, the high-speed, high-resolution volumetric imaging capabilities of SPED light sheet microscopy may be helpful across diverse domains of life science research which are increasingly dependent on the ability to rapidly capture tissue events and elements within large intact volumes.

EXPERIMENTAL PROCEDURES

SPED Light Sheet Implementation
SPED light sheet microscopy prototype was built on the previously described COLM (Tomer et al., 2014) backbone, which provides an efficient platform for testing diverse refractive indices and thicknesses of RI blocks as a layer of liquid between the sample and the detection objective. Figure 2 shows the details of SPED optical implementation. Briefly, two light sheets are generated from two opposite illumination arms that include a laser source, filter wheel, shutter, x-y galvanometer scanner, scan lens, tube lens, mirror, and the illumination objective (Olympus Macro 4×/0.28 NA). The emitted signal is detected with an orthogonally arranged wide-field detection arm, including a detection objective, emission filter wheel, tube lens, and sCMOS camera (Hamamatsu Orca Flash 4.0 V2). Details of these parts were described previously (Tomer et al., 2014). Note that we rotated the detection camera by 90 degrees (i.e., camera rows were orthogonal to the illumination beam propagation direction) for live imaging experiments to maximize the data acquisition speed by minimizing the number of rows that were needed to cover the samples. For the 12 volume per second whole-brain imaging, this resulted in isolated visual line artifacts on the sample periphery in Movie S6. Refractive index (RI) blocks to induce spherical aberration-based axial PSF elongation (SPED) were implemented by filling the sample chamber (Figure 2) with specific refractive index liquids (1.454 was used for the most of the experiments). The RI block thickness was specified using variable lengths of lens tubes (Thorlabs, 2" diameter)

in the sample chamber (Figure 2). This is equivalent to using solid transparent material of varying thickness. Samples were mounted in custom thin-walled (0.5-mm-thick) quartz glass cuvettes (Starna Cells). The imaging procedures for rapid light sheet scanning (while keeping all the other parts stationary) and time lapse experiment data logging were implemented in the previously described (Tomer et al., 2014) COLM software and electronics control framework.

Experimental PSFs and Analysis
We used 1 μm diameter beads to assess the PSF of diverse objectives in the SPED light sheet versus standard air imaging configurations. PSFs were recorded by synchronously moving the beads and the light sheet (typically in a z step of 4 μm), so that the beads remained constantly and uniformly illuminated throughout the image stacks. Beads were manually identified and cropped using Fiji (Schindelin et al., 2012), were up-sampled 2-fold, and aligned rigidly (with six parameters: three for translation and three for rotation) in Amira (FEI). Final average PSFs were generated by taking an average of the normalized (by subtracting mean signal, and dividing by the SD) images of all beads (n ≥ 5). Lateral PSF FWHMs as a function of z position were calculated by subtracting the average background level, identifying the bead center in each slice center, and then averaging the FWHM of four cross sections through this center position.

SPED Light Sheet PSF Simulations
The effect of various SPED light sheet system parameters on the PSF extension was assessed by optical simulations performed using Zemax OpticStudio 13 (Kirkland, WA). The FFT PSF function, which includes the influence of wave-optics for numerical apertures up to approximately 0.4, was used for all simulations. The optical prescription is presented in Figure S2A. In brief, the objective and the tube lens were approximated as ideal (paraxial) lenses, and focal lengths were set according to the working distance and the overall system magnification. The numerical aperture (NA) was set as a system parameter that controlled the size of an aperture stop at the back focal plane of the objective lens. This optical prescription allowed access to all the system
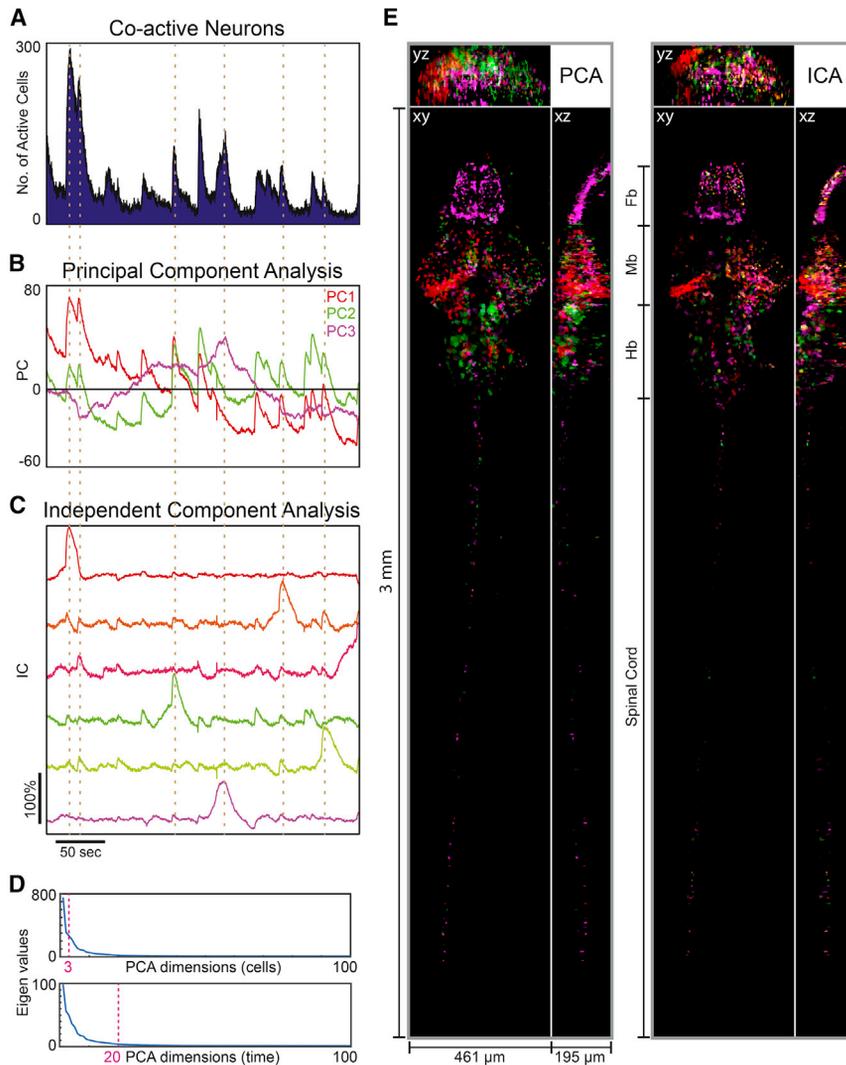
Figure 7. Population Analysis of Global Zebrafish CNS Activity Recorded by SPED Light Sheet Microscopy

Principal component analysis (PCA) and independent component analysis (ICA) were used to analyze the population dynamics of neurons spread across the entire zebrafish larval CNS. The dataset was acquired using a 4×/0.28 NA objective at 6.23 volumes/sec (as in Figure 6A). ΔF/F activity profiles of all cells were first filtered to identify active neurons by choosing a noise level corresponding to 5% false positive rate as the cutoff, followed by PCA and ICA; early time points that may represent nonspecific responses to initial laser illumination were excluded from analysis.

(A) Number of co-active neurons as a function of time across the recording duration.

(B) Temporal traces of top three principal components (PC) shown in red, green and magenta respectively. y axis represents arbitrary units in PCA space.

(C) Temporal traces of 6 recovered independent components (IC) out of 10 (filtered to retain traces in which the sum of minimum and maximum values was greater than zero); units are arbitrary. The dotted lines across panels indicate peaks in the ICs that correspond to the peaks in PCA and cellular activity.

(D) Eigenvalues for the top 100 dimensions of cellular (top) and time points (bottom) principal components. Dashed lines mark the top 3 cellular and the top 20 temporal PCA dimensions, which were used in (B) and for data "whitening" before ICA (methods) in (C).

(E) Spatial plots of each PC coefficient (absolute value) and each IC (absolute value) were generated to visualize the locations and identities of the neurons associated with each component. Different components were combined into multicolor images (each color corresponding to coloring of the temporal traces in B and C) after scaling for contrast. Images shown are maximum intensity projections through x, y or z. Fb, Forebrain; Mb, midbrain, Hb, Hindbrain.

parameters: (i) the refractive index of the material in which the sample was embedded and the sample z position, (ii) the thickness and the refractive index of the coverglass separating the sample from the RI liquid, (iii) the thickness and refractive index of the RI liquid block, (iv) the thickness and refractive index of a coverglass between the RI liquid and the objective, and (v) the thickness of the air gap between the objective and the cover glass. All the surfaces, before the objective, were set to infinite flat curvature. The distance between the tube lens and the sensor was varied for refocusing the position of the camera sensor. We used a custom macro to sequentially step the z position of the object (in 10 microns steps) to generate the 3D PSF, and wrote custom Python scripts to process the Zemax output files.

Imaging Experiments

The clarified adult mouse brain sample was generated from a *Thy1-eYFP* transgenic mouse, using the methods described previously in detail (Tomer et al., 2014). The clarified brain sample was incubated in 65% glycerol and mounted in a quartz cuvette for SPED light sheet and standard COLM imaging. Live 10 dpf larval zebrafish, expressing nuclear-localized GCaMP6s Tg(*elavl3: H2B-GCaMP6s*), were mounted in a quartz cuvette (Tomer et al., 2014) and immobilized in a layer of 1% low melting point agarose (Sigma) in the corner of the cuvette, which was then filled with fish system water. SPED light sheet microscopy under different configurations was performed by step-wise rapid scanning of the light sheet and detecting the corresponding illuminated planes with an sCMOS (Orca Flash 4.0 V2) camera. Uni-directional rolling shutter mode was used for acquiring anatomy images, and the standard bi-directional mode for live imaging experiments. A z step of 2 or 4 μm was used for the anatomy images shown in Figure 4. For live imaging, a z step of 5 μm was used to cover the entire depth in 40 slices. Light sheets used for the imaging experiments were 4 to 6 μm thick. All imaging experiments were performed with one side light sheet illumination. For LFM data collection, 10 dpf Tg(*elavl3:H2B-GCaMP6s*) larvae were immobilized in 2% low melting point agarose (Sigma) and placed on a standard petri dish filled with fish system water. LFM was performed on a Leica SP5 using a 10×/0.6NA Olympus water-dipping objective modified to have a 250 mm focal length tube lens, f/11.36 100 μm pitch microlens array (Jenoptics), and Andor Zyla sCMOS camera attached to the wide-field imaging port. Fish were imaged at 2 Hz for 5 min using 2.3 mW light power (excitation: 450–490 nm; dichroic: 495 nm long-pass; emission: 500–550 nm). Light field images were transferred to Amazon Web Services S3, and volumes were reconstructed using the 3D deconvolution algorithm described previously (Broxton et al., 2013) on a GPU cluster within Amazon's Elastic Compute Cloud (EC2). Volumes were reconstructed with a voxel size of 3.6 × 3.6 × 5 μm.

Deconvolution Pipeline

The SPED data deconvolution pipeline is described in detail in Figure S4. Standard Richardson-Lucy implementation in Matlab (Matlab R2015a, The MathWorks, Natick, MA) was used for performing the deconvolution. As a first step, a system empirical PSF (for the objective used for acquiring the dataset) was aligned (along the z axis) with the raw image stack. To achieve this, a subset of z slices (typically separated by 100 μm) was deconvolved with a set of 2D PSFs uniformly sampled across the depth (along the z axis, typically separated by 10 μm) of the 3D system PSF. The resulting images were inspected manually for sharpness to determine global mapping of the system PSF with the raw image stack (Figure S4, step 1). The aligned PSF was then used to deconvolve all the z slices by 2D PSF image at corresponding mapped z positions (Figure S4, step 2). Typically 10–20 iterations were used for the Richardson-Lucy deconvolution. Computation time of ~4 s was needed to deconvolve a 2,048 × 1,111 pixels size image with ten iterations on a single core of Intel/Xeon/E5-2687W/3.10 GHz processor. For the time lapse recordings, step 1 of aligning the PSF to the dataset was performed using the first time point. The resulting mapped PSF was then used to deconvolve all the time points (second step). Data acquired by 4×/0.28NA objective (Olympus) were up-sampled 2-fold (using bi-cubic interpolation) before deconvolution. All datasets presented have been deconvolved using the pipeline described above, unless explicitly identified as raw data.

Image Segmentation and Quantitative Analysis

All image segmentation and quantitative analyses were performed using Matlab (R2015a, The MathWorks, Natick, MA) and the DIPimage toolbox (version 2.7) and R. ΔF/F (Yuste and Katz, 1991) of live functional imaging datasets was calculated as follows. First, a reference 3D image (corresponding to baseline F) was generated by averaging all the time points. 3D ΔF/F images were then calculated by using the formula: $((Fs - Fb * 0.6/Fb + 10) + 1) * 5000$, where Fs is the signal and Fb is the baseline. (Note that, because of the requirement for interpolation between consecutive z slices and the up-scaling, minor visual line artifacts can be observed in the x-z and y-z projections in the Movies S5, S6, and S7.) Image segmentation to identify cells was performed on the SD (voxel-wise, across entire time series) of the deconvolved datasets. In brief, a local intensity normalization operation was applied to the image volume, and a marker-based watershed approach was then used to label all the cells. Traces for all the segmented cells were calculated by overlapping the labeled (after segmentation) volumes over the time-lapse datasets. For PCA analysis, ΔF/F traces of each datasets were first filtered to identify all the active cells in the recording durations. To achieve this, ΔF/F noise for each cell was estimated as follows. Each ΔF/F trace was normalized by subtracting the mean and dividing by the mean of the trace. For identifying activity signals, we determined a local cutoff for each of the normalized ΔF/F traces, by subjecting them to a recursive algorithm to identify a noise level cut-off corresponding to 5% false positive rate, as described in detail previously (Dombeck et al., 2007; Lovett-Barron et al., 2014; Rajasethupathy et al., 2015). The filtered traces were then subjected to principal component analysis (PCA, using princomp function in Matlab) and independent component analysis (ICA, using the fastICA Matlab implementation; Hyvärinen et al., 2001). As is standard for fast ICA (Hyvärinen et al., 2001), data were "whitened" prior to ICA using the first 20 principal components (see Figure 7D for PCA eigenvalues), and ICA was randomly initialized. The number of independent components was set to ten, resulting in six components for which the sum of minimum and maximum values was greater than zero. These six components are displayed in Figure 7.

SUPPLEMENTAL INFORMATION

Supplemental Information includes six figures, eight movies, and one data file and can be found with this article online at http://dx.doi.org/10.1016/j.cell.2015.11.061.

AUTHOR CONTRIBUTIONS

R.T. developed the SPED light sheet microscopy, and with K.D. designed the experiments. R.T. and M.L.B performed the SPED zebrafish imaging, and R.T. performed all the other experiments. R.T. developed the image processing framework and analyzed all the data. A.A. and V.B. contributed to empirical PSF quantification. I.K. and R.T. performed the PSF simulations with input from S.Y. A.A. and S.S. contributed to the scripts for analysis. L.G., M.B., S.Y. and A.A. led the light field microscopy development with its associated image processing. A.A. and V.B. performed the LFM imaging. R.T. and K.D. wrote the paper with editorial input from all authors. K.D. supervised all aspects of the work.

REFERENCES

Abrahamsson, S., Chen, J., Hajj, B., Stallinga, S., Katsov, A.Y., Wisniewski, J., Mizuguchi, G., Soule, P., Mueller, F., Dugast Darzacq, C., et al. (2013). Fast multicolor 3D imaging using aberration-corrected multifocus microscopy. Nat. Methods 10, 60–63.

Abrahamsson, S., McQuilken, M., Mehta, S.B., Verma, A., Larsch, J., Ilic, R., Heintzmann, R., Bargmann, C.I., Gladfelter, A.S., and Oldenbourg, R. (2015). MultiFocus Polarization Microscope (MF-PolScope) for 3D polarization imaging of up to 25 focal planes simultaneously. Opt. Express 23, 7734–7754.

Ahrens, M.B., Orger, M.B., Robson, D.N., Li, J.M., and Keller, P.J. (2013). Whole-brain functional imaging at cellular resolution using light-sheet microscopy. Nat. Methods 10, 413–420.

Bouchard, M.B., Voleti, V., Mendes, C.S., Lacefield, C., Grueber, W.B., Mann, R.S., Bruno, R.M., and Hillman, E.M. (2015). Swept confocally-aligned planar excitation (SCAPE) microscopy for high speed volumetric imaging of behaving organisms. Nat. Photonics 9, 113–119.

Broxton, M., Grosenick, L., Yang, S., Cohen, N., Andalman, A., Deisseroth, K., and Levoy, M. (2013). Wave optics theory and 3-D deconvolution for the light field microscope. Opt. Express 21, 25418–25439.

Chen, T.W., Wardill, T.J., Sun, Y., Pulver, S.R., Renninger, S.L., Baohan, A., Schreiter, E.R., Kerr, R.A., Orger, M.B., Jayaraman, V., et al. (2013). Ultrasensitive fluorescent proteins for imaging neuronal activity. Nature 499, 295–300.

Chen, B.C., Legant, W.R., Wang, K., Shao, L., Milkie, D.E., Davidson, M.W., Janetopoulos, C., Wu, X.S., Hammer, J.A., 3rd, Liu, Z., et al. (2014). Lattice light-sheet microscopy: imaging molecules to embryos at high spatiotemporal resolution. Science 346, 1257998.

Chen, F., Tillberg, P.W., and Boyden, E.S. (2015). Optical imaging. Expansion microscopy. Science 347, 543–548.

Chhetri, R.K., Amat, F., Wan, Y., Höckendorf, B., Lemon, W.C., and Keller, P.J. (2015). Whole-animal functional and developmental imaging with isotropic spatial resolution. Nat. Methods 12, 1171–1178.

Chung, K., Wallace, J., Kim, S.Y., Kalyanasundaram, S., Andalman, A.S., Davidson, T.J., Mirzabekov, J.J., Zalocusky, K.A., Mattis, J., Denisin, A.K.,

et al. (2013). Structural and molecular interrogation of intact biological systems. Nature *497*, 332–337.

Cohen, N., Yang, S., Andalman, A., Broxton, M., Grosenick, L., Deisseroth, K., Horowitz, M., and Levoy, M. (2014). Enhancing the performance of the light field microscope using wavefront coding. Opt. Express *22*, 24817–24839.

Deisseroth, K. (2015). Optogenetics: 10 years of microbial opsins in neuroscience. Nat. Neurosci. *18*, 1213–1225.

Dombeck, D.A., Khabbaz, A.N., Collman, F., Adelman, T.L., and Tank, D.W. (2007). Imaging large-scale neural activity with cellular resolution in awake, mobile mice. Neuron *56*, 43–57.

Dunsby, C. (2008). Optically sectioned imaging by oblique plane microscopy. Opt. Express *16*, 20306–20316.

Fahrbach, F.O., Voigt, F.F., Schmid, B., Helmchen, F., and Huisken, J. (2013). Rapid 3D light-sheet microscopy with a tunable lens. Opt. Express *21*, 21010–21026.

Freeman, J. (2015). Open source tools for large-scale neuroscience. Curr. Opin. Neurobiol. *32*, 156–163.

Freeman, J., Vladimirov, N., Kawashima, T., Mu, Y., Sofroniew, N.J., Bennett, D.V., Rosen, J., Yang, C.T., Looger, L.L., and Ahrens, M.B. (2014). Mapping brain activity at scale with cluster computing. Nat. Methods *11*, 941–950.

Gao, L., Shao, L., Higgins, C.D., Poulton, J.S., Peifer, M., Davidson, M.W., Wu, X., Goldstein, B., and Betzig, E. (2012). Noninvasive imaging beyond the diffraction limit of 3D dynamics in thickly fluorescent specimens. Cell *151*, 1370–1385.

Grosenick, L., Anderson, T., and Smith, S.J. (2009). Elastic Source Selection for in vivo imaging of neuronal ensembles. Biomedical Imaging: From Nano to Macro, 2009 ISBI '09 IEEE International Symposium on *June 28 2009-July 1 2009*, 1263 - 1266.

Holekamp, T.F., Turaga, D., and Holy, T.E. (2008). Fast three-dimensional fluorescence imaging of activity in neural populations by objective-coupled planar illumination microscopy. Neuron *57*, 661–672.

Huisken, J., Swoger, J., Del Bene, F., Wittbrodt, J., and Stelzer, E.H. (2004). Optical sectioning deep inside live embryos by selective plane illumination microscopy. Science *305*, 1007–1009.

Hyvärinen, A., Karhunen, J., and Oja, E. (2001). Independent Component Analysis (John Wiley & Sons).

Keller, P.J., Schmidt, A.D., Wittbrodt, J., and Stelzer, E.H. (2008). Reconstruction of zebrafish early embryonic development by scanned light sheet microscopy. Science *322*, 1065–1069.

Keller, P.J., Ahrens, M.B., and Freeman, J. (2015). Light-sheet imaging for systems neuroscience. Nat. Methods *12*, 27–29.

Lemon, W.C., Pulver, S.R., Höckendorf, B., McDole, K., Branson, K., Freeman, J., and Keller, P.J. (2015). Whole-central nervous system functional imaging in larval Drosophila. Nat. Commun. *6*, 7924.

Lerner, T.N., Shilyansky, C., Davidson, T.J., Evans, K.E., Beier, K.T., Zalocusky, K.A., Crow, A.K., Malenka, R.C., Luo, L., Tomer, R., and Deisseroth, K. (2015). Intact-Brain Analyses Reveal Distinct Information Carried by SNc Dopamine Subcircuits. Cell *162*, 635–647.

Levoy, M., Ng, R., Adams, A., Footer, M., and Horowitz, M. (2006). Light Field Microscopy. Proc SIGGRAPH *25*.

Lovett-Barron, M., Kaifosh, P., Kheirbek, M.A., Danielson, N., Zaremba, J.D., Reardon, T.R., Turi, G.F., Hen, R., Zemelman, B.V., and Losonczy, A. (2014). Dendritic inhibition in the hippocampus supports fear learning. Science *343*, 857–863.

Panier, T., Romano, S.A., Olive, R., Pietri, T., Sumbre, G., Candelier, R., and Debrégeas, G. (2013). Fast functional imaging of multiple brain regions in intact zebrafish larvae using selective plane illumination microscopy. Front. Neural Circuits *7*, 65.

Pitrone, P.G., Schindelin, J., Stuyvenberg, L., Preibisch, S., Weber, M., Eliceiri, K.W., Huisken, J., and Tomancak, P. (2013). OpenSPIM: an open-access light-sheet microscopy platform. Nat. Methods *10*, 598–599.

Planchon, T.A., Gao, L., Milkie, D.E., Davidson, M.W., Galbraith, J.A., Galbraith, C.G., and Betzig, E. (2011). Rapid three-dimensional isotropic imaging of living cells using Bessel beam plane illumination. Nat. Methods *8*, 417–423.

Preibisch, S., Saalfeld, S., Schindelin, J., and Tomancak, P. (2010). Software for bead-based registration of selective plane illumination microscopy data. Nat. Methods *7*, 418–419.

Prevedel, R., Yoon, Y.G., Hoffmann, M., Pak, N., Wetzstein, G., Kato, S., Schrödel, T., Raskar, R., Zimmer, M., Boyden, E.S., and Vaziri, A. (2014). Simultaneous whole-animal 3D imaging of neuronal activity using light-field microscopy. Nat. Methods *11*, 727–730.

Quirin, S., Peterka, D.S., and Yuste, R. (2013). Instantaneous three-dimensional sensing using spatial light modulator illumination with extended depth of field imaging. Opt. Express *21*, 16007–16021.

Quirin, S., Jackson, J., Peterka, D.S., and Yuste, R. (2014). Simultaneous imaging of neural activity in three dimensions. Front. Neural Circuits *8*, 29.

Rajasethupathy, P., Sankaran, S., Marshel, J.H., Kim, C.K., Ferenczi, E., Lee, S.Y., Berndt, A., Ramakrishnan, C., Jaffe, A., Lo, M., et al. (2015). Projections from neocortex mediate top-down control of memory retrieval. Nature *526*, 653–659.

Reynaud, E.G., Peychl, J., Huisken, J., and Tomancak, P. (2015). Guide to light-sheet microscopy for adventurous biologists. Nat. Methods *12*, 30–34.

Schindelin, J., Arganda-Carreras, I., Frise, E., Kaynig, V., Longair, M., Pietzsch, T., Preibisch, S., Rueden, C., Saalfeld, S., Schmid, B., et al. (2012). Fiji: an open-source platform for biological-image analysis. Nat. Methods *9*, 676–682.

Siedentopf, H., and Zsigmondy, R. (1903). Uber Sichtbarmachung und Grössenbestimmung ultramikroskopischer Teilchen, mit besonderer Anwendung auf Goldrubingläser. Ann. Phys. *10*, 1–39.

Stelzer, E.H. (2015). Light-sheet fluorescence microscopy for quantitative biology. Nat. Methods *12*, 23–26.

Tomer, R., Ye, L., Hsueh, B., and Deisseroth, K. (2014). Advanced CLARITY for rapid and high-resolution imaging of intact tissues. Nat. Protoc. *9*, 1682–1697.

Truong, T.V., Supatto, W., Koos, D.S., Choi, J.M., and Fraser, S.E. (2011). Deep and fast live imaging with two-photon scanned light-sheet microscopy. Nat. Methods *8*, 757–760.

Vladimirov, N., Mu, Y., Kawashima, T., Bennett, D.V., Yang, C.T., Looger, L.L., Keller, P.J., Freeman, J., and Ahrens, M.B. (2014). Light-sheet functional imaging in fictively behaving zebrafish. Nat. Methods *11*, 883–884.

Wolf, S., Supatto, W., Debrégeas, G., Mahou, P., Kruglik, S.G., Sintes, J.M., Beaurepaire, E., and Candelier, R. (2015). Whole-brain functional imaging with two-photon light-sheet microscopy. Nat. Methods *12*, 379–380.

Wu, Y., Wawrzusin, P., Senseney, J., Fischer, R.S., Christensen, R., Santella, A., York, A.G., Winter, P.W., Waterman, C.M., Bao, Z., et al. (2013). Spatially isotropic four-dimensional imaging with dual-view plane illumination microscopy. Nat. Biotechnol. *31*, 1032–1038.

Yuste, R., and Katz, L.C. (1991). Control of postsynaptic Ca2+ influx in developing neocortex by excitatory and inhibitory neurotransmitters. Neuron *6*, 333–344.
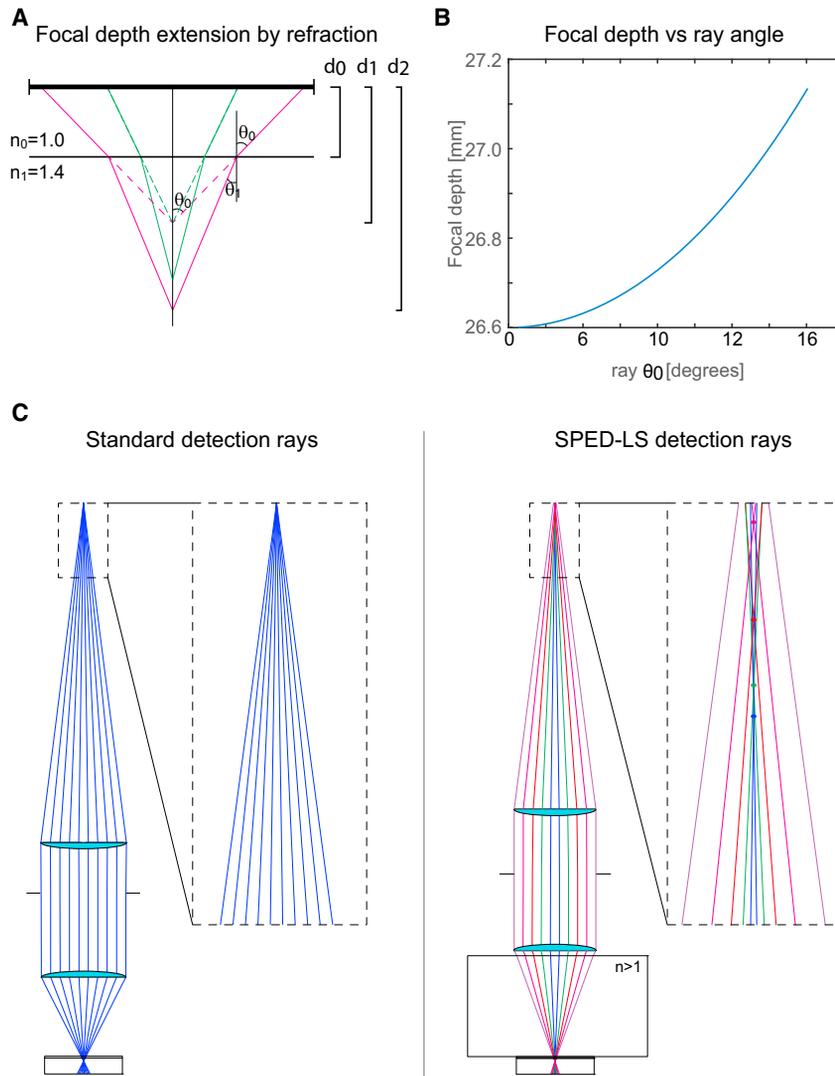
Figure S1. Optical Mechanisms Underlying SPED Light Sheet Microscopy, Related to Figure 1

Spherical aberrations elongate the PSF by focusing rays that pass through different parts of the objective aperture at different distances. (A) Ray tracing example to demonstrate the extension of depth of focus caused by introduction of a high refractive index material in the optical path. (B) Relationship between the incidence ray angle (the sine of which defines the numerical aperture) and the focal depth, demonstrating PSF elongation by the introduction of a block of high refractive index material. (C) Comparative ray tracing of normal (aberration-free) and SPED detection systems, demonstrating elongation of the PSF achieved in SPED light sheet.
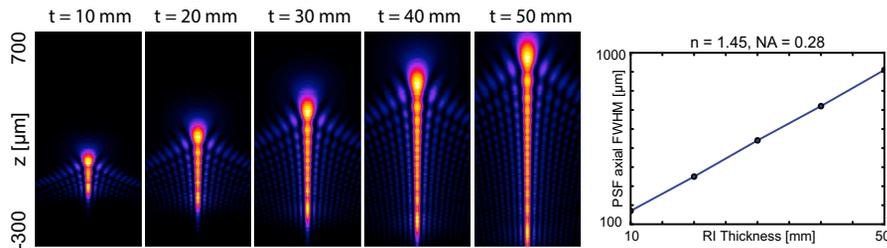
A Zemax optical prescription used for SPED-LS PSF simulations

	Comment	Radius	Thickness	Glass
OBJ	sample medium	inf	z+0.75	1.33
2	cover glass	inf	0.5	1.45
3	RI material	inf	10 to 50	1 to 1.7
4	cover glass	inf	0.1	1.45
5	air gap	inf	1	1.00
6	objective		f_obj	
STO	stop	inf	f_tl	1.00
8	tube lens		sensor dist	
IMA	sensor	inf		1.00

B Effect of Block refractive index
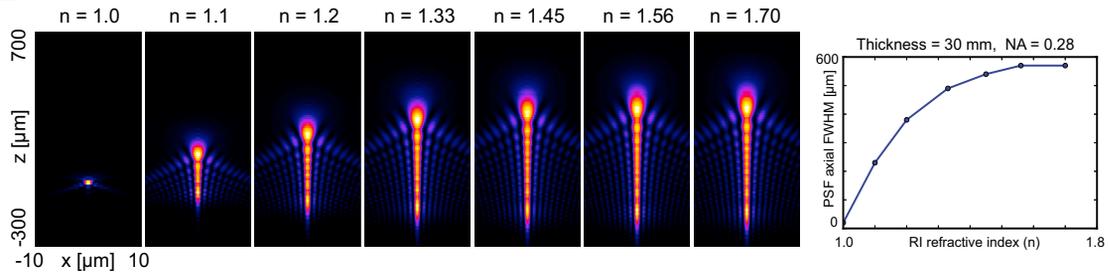
C Effect of Block thickness

D Effect of detection objective NA
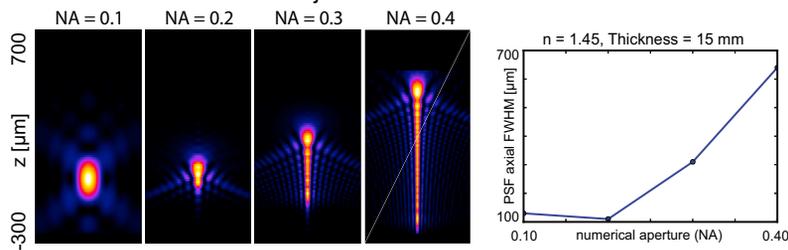
Figure S2. SPED Light Sheet PSF Simulations to Identify Crucial Tuning Parameters, Related to Figure 1

The detection arm of SPED-LS was modeled in Zemax using the optical prescription shown in (A). Note that the simulation design assumes ideal lenses, and thus estimated FWHMs may not necessarily exactly match the empirically measured PSFs; the simulations do, however, describe the general trends associated with varying system parameters. See Experimental Procedures for further details. (B-D) assess the effects of changing the refractive index (RI) of the block, its thickness and the numerical aperture (NA) of the detection objective, respectively. As summarized in the graphs, the PSF elongation increases with corresponding increases in all three parameters: linearly with block thickness, and non-linearly with RI and detection objective NA.
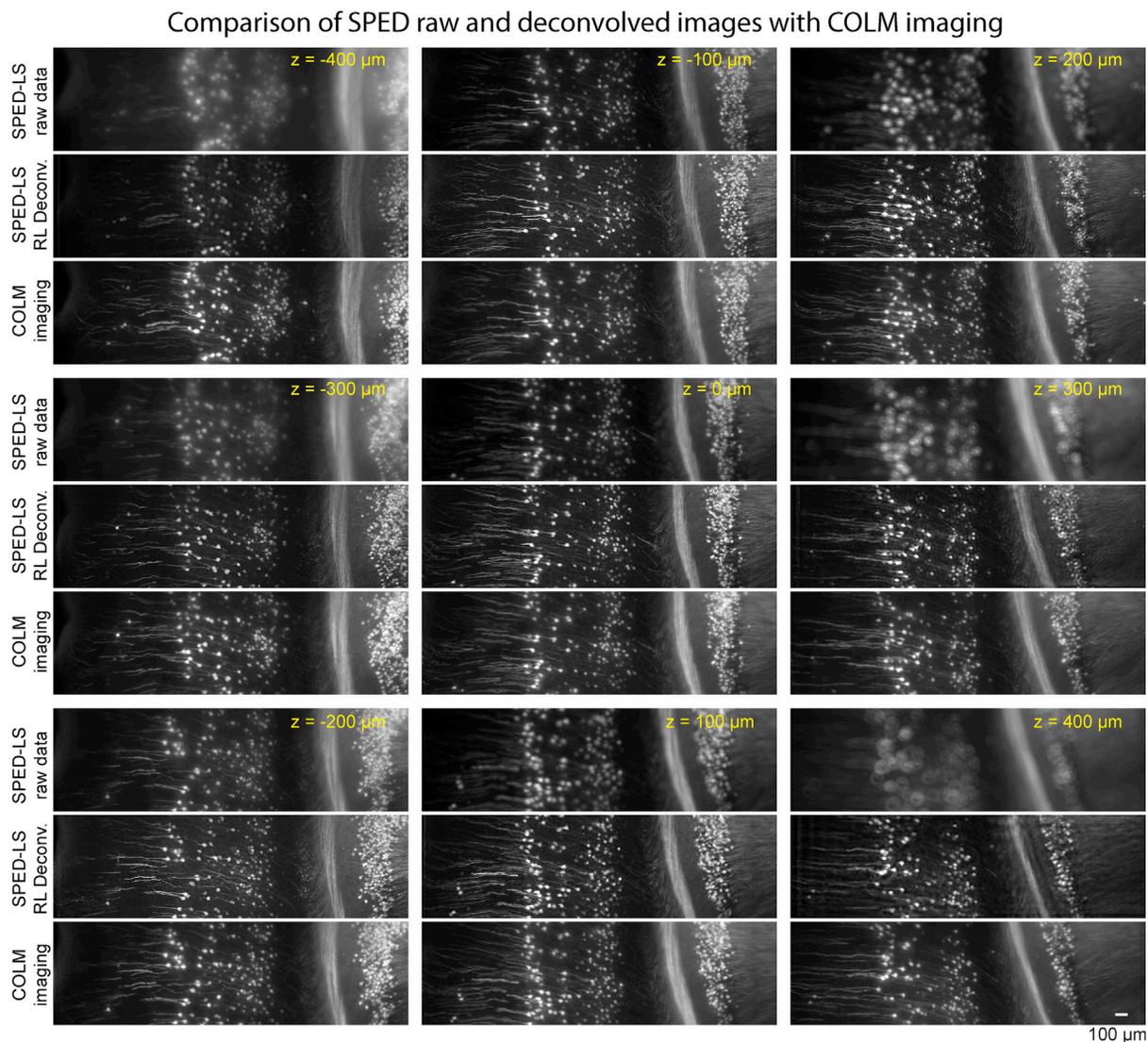
Comparison of SPED raw and deconvolved images with COLM imaging

Figure S3. Comparison of SPED Light Sheet Microscopy with Standard COLM Imaging, Related to Figure 3

A consecutive series of optical sections (100 μm thick) is shown to demonstrate the volumetric imaging capability of SPED light sheet microscopy. Image volumes were acquired by SPED or COLM, using a 4×/0.28NA detection objective, of the same sample volume of clarified *Thy1–eYFP* transgenic mouse brain. Each panel shows SPED raw and deconvolved images and the corresponding optical sections from the COLM stack. The z axis positions (middle of the stack set to 0 μm) are labeled in yellow, marking the position of the middle of the 100-μm-thick optical sections. Detailed volume rendering of the image stack is shown in Figure 3C and Movie S2. Scale bar, 100 μm.

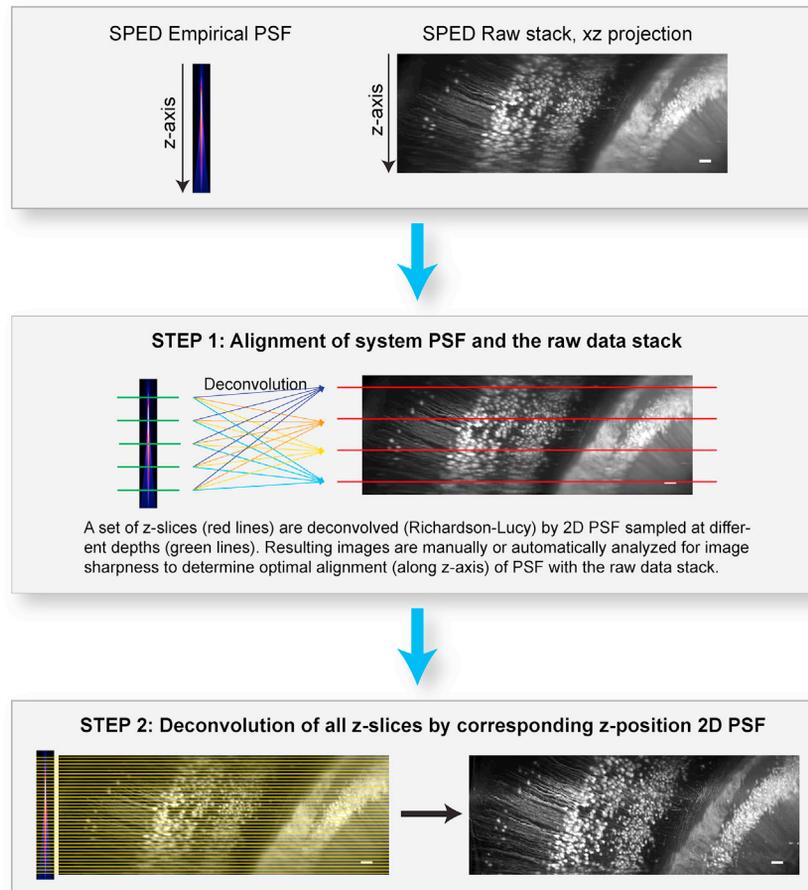## SPED light sheet microscopy data deconvolution pipeline

Figure S4. SPED Light Sheet Data Deconvolution Pipeline, Related to Figure 3

Schematics summarizing the SPED data deconvolution pipeline. In the first step, the empirically determined system PSF is aligned (along z axis) with the raw data stack. This is achieved by performing deconvolution (Richardson-Lucy) of a small number of z slices (typically separated by 100 μm) of data with a set of 2D PSFs sampled at different depths (typically separated by 10 μm). The resulting deconvolved images are analyzed (manually or automatically) for sharpness to determine the global z axis alignment of the system PSF and the raw data stack. In the second step, all the z slices of the image stack are deconvolved using 2D PSFs sampled from system PSF at correspondingly aligned z positions. For time-lapse datasets, PSF and stack alignment is calculated using the first time point data, which is then used to deconvolve all the time points (second step). Scale bar, 100 μm.

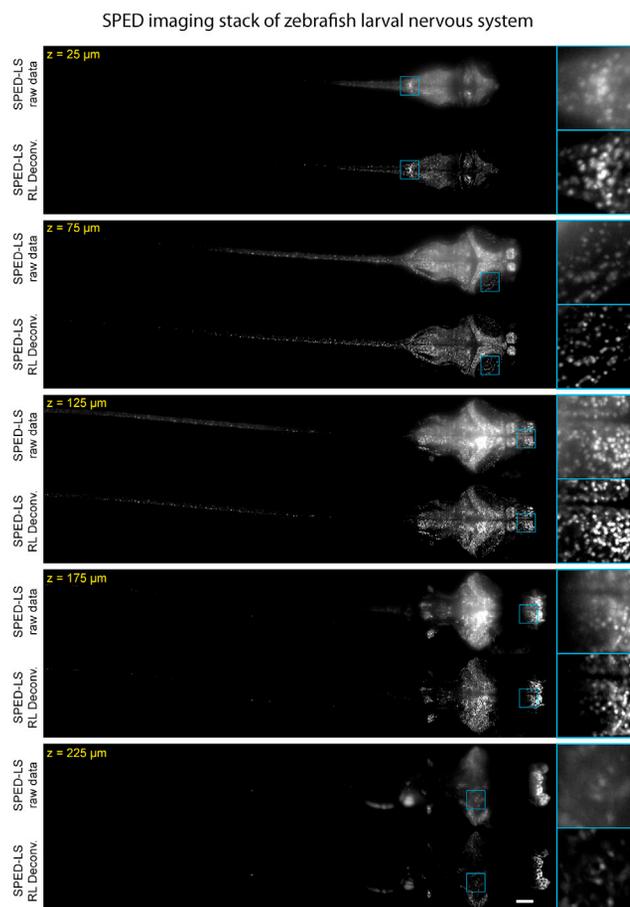SPED imaging stack of zebrafish larval nervous system

Figure S5. Comparison of Raw and Deconvolved SPED Light Sheet Data Stack, Related to Figure 4

A consecutive series of optical sections (50 μm thick) is shown to demonstrate image quality enhancement after deconvolution. Data were acquired from a 10 dpf Tg(*elavl3:H2B-GCaMP6s*) zebrafish larva using 4×/0.28NA detection objective. Image volumes of 10 consecutive time points (arbitrarily chosen number to increase labeled cell count) were combined into one volume by taking the maximum values of the voxels across the time points. Detailed volume rendering of the image stack is shown in Figure 3A and Movie S3. Scale bar, 100 μm.
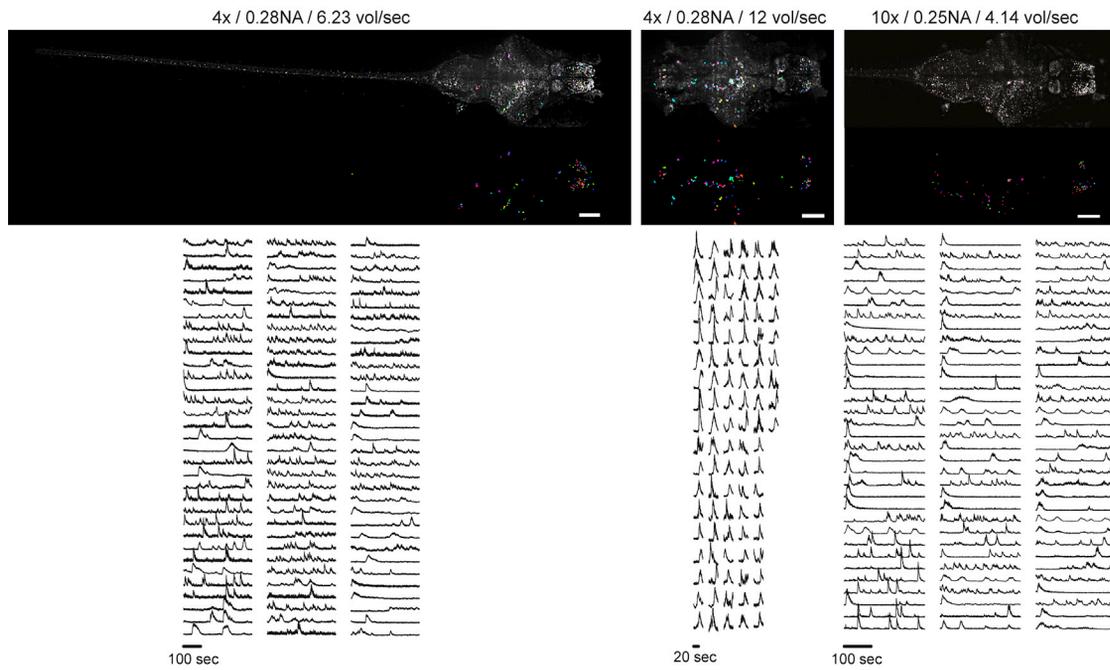
Activity time series traces of 99 most active neurons

Figure S6. Neuronal Activity Time Series across the Intact Nervous System, Related to Figure 6

Neuronal activity traces (ΔF/F) are shown for top 99 most active neurons in the larval zebrafish nervous system (assessed by variance across the entire recording duration), imaged using 4×/0.28 NA objective at 6.23 volumes/second (3 mm × 0.5 mm × 0.2 mm, 39 z slices), 4×/0.28 NA objective at 12 volumes per second (0.9 mm × 0.4 mm × 0.2 mm, 40 z slices) and 10×/0.25 NA objective at 4.14 volumes per second (1.2 mm × 0.43 mm × 0.2 mm, 39 z slices). Spatial distribution of identified cells is overlaid on the maximum intensity projection image of voxel-wise SD across the entire recording duration. Scale bars, 100 μm.